

Supplementary Materials for

Filamentous active matter: Band formation, bending, buckling, and defects

Gerard A. Vliegenthart*, Arvind Ravichandran, Marisol Ripoll, Thorsten Auth, Gerhard Gompper

*Corresponding author. Email: g.vliegenthart@fz-juelich.de

Published 24 July 2020, *Sci. Adv.* **6**, eaaw9975 (2020)

DOI: [10.1126/sciadv.aaw9975](https://doi.org/10.1126/sciadv.aaw9975)

The PDF file includes:

Legends for movies S1 to S5

Figs. S1 to S11

References

Other Supplementary Material for this manuscript includes the following:

(available at advances.sciencemag.org/cgi/content/full/6/30/eaaw9975/DC1)

Movies S1 to S5

Band formation and steady-state structure at large persistence lengths or low activity

Figure S1 shows the time evolution of a nematic phase with large persistence length when motors are added. At short times (a) the system is in a disordered nematic state. At intermediate times (b) the system forms polar-sorted bands that subsequently coarsen, and at late times (c), when the system reaches steady state, two stable oppositely aligned bands form. This is a typical time sequence for large persistence lengths and/or for small activities.

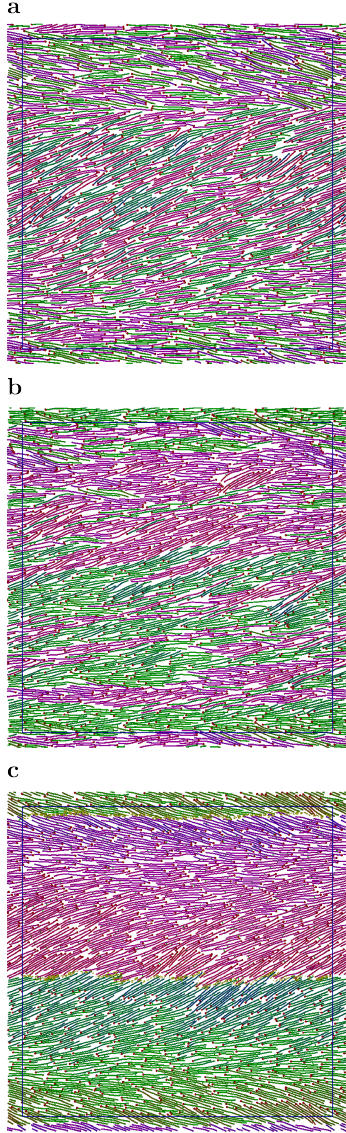


fig. S1. Time sequence of filament self-organisation. Here, $(\phi, \tilde{\ell}_p, \tilde{n}_m) = (0.66, 20, 0.89)$, with time $\tilde{t} = tD_0/L^2$ and D_0 the passive single filament diffusion coefficient. (a) $\tilde{t} = 0$, nematic phase at zero activity; (b) $\tilde{t} = 0.0125$ polarity sorting; (c) $\tilde{t} = 2.5$ stationary state consisting of two stable bands.

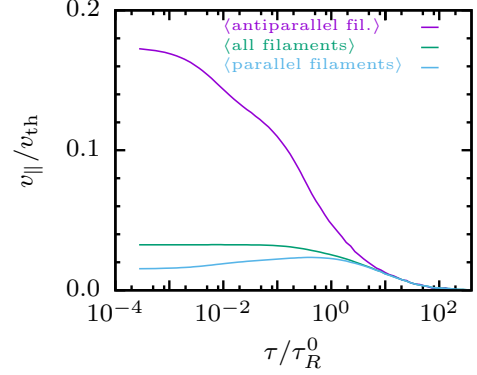


fig. S2. Normalised parallel velocity $v_{||}/v_{th}$. Parallel velocity as a function of lag time τ/τ_R^0 for $(\phi, \tilde{\ell}_p, \tilde{n}_m) = (0.66, 3.4, 0.89)$. Here $v_{th} = \sqrt{k_B T/m}$. Averages are shown for all filaments, for parallel filaments only, and for antiparallel filaments only.

Parallel velocity and temporal orientational autocorrelation function

Figure S2 shows the parallel velocity averaged over all filaments as a function of the lag time τ . The average is also performed over only the filaments in a parallel environment (filaments point in the same direction), and in an antiparallel environment (filaments at the interface point in opposite direction) filaments. Clearly, the velocity of the antiparallel filaments is much larger than that of the parallel ones. The average velocity over all filaments is closer to the average over the parallel filaments because the fraction of parallel filaments is much larger. In each domain, parallel filaments form the bulk of the domain interior, while antiparallel filaments are found at the boundaries.

Intradomain dynamics

Our component-based model provides detailed microscopic information about the filament dynamics within the polar domains. We studied configurations with a stable number of bands, an example is shown in fig. S3a. The corresponding velocity profiles are calculated for various values of the active force by changing the number of motors per filament $\tilde{n}_m = n_m/n_f$, see fig. S3b. The average band velocity increases linearly with the number of antiparallel motors n_m^{ap} , in agreement with the results in fig. 1f. The total length of the interface, $L_{inter} \simeq n_b L_{box}$, varies by changing the number of bands, or by enlarging the box size. The band velocity is roughly independent of the persistence length, see fig. S3c, which indicates that the interfacial structure is not dramatically affected by the filament flexibility.

Our results demonstrate that the force applied by the antiparallel motors at the interfaces generates the motion of the bands. The parallel motors connecting filaments

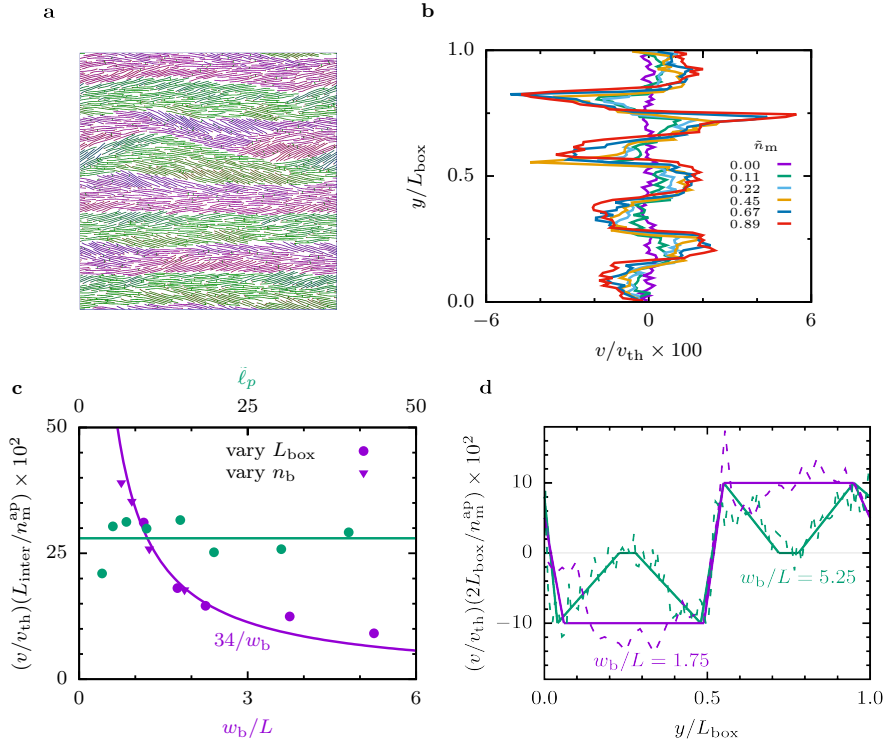


fig. S3. Intra-band filament dynamics for narrow and wide bands at steady state.

(a) Snapshots for a system with parallel bands for $(\phi, \ell_p, n_b, \tilde{n}_m) = (0.66, 20, 8, 0.12)$. (b) Velocity profiles for various \tilde{n}_m . $(\phi, \tilde{\ell}_p, n_b) = (0.66, 20, 8)$ (c) Normalised averaged band velocities as a function of the band width w_b and the persistence length ℓ_p of the filaments for $(n_b, \tilde{n}_m) = (6, 0.45)$. The antiparallel motor density is $n_m^{\text{ap}}/L_{\text{inter}}$ where $L_{\text{inter}} = n_b L_b$ is the total length of the interface in the system. (d) Normalised velocity profiles for two band widths. Dashed lines are simulation results and solid lines are guides to the eye.

within the bands transmit this force in the perpendicular direction, but the friction with the embedding medium strongly reduces the velocity in the center of the wide bands. From the velocity profile for the wide bands, see fig. S3 d, we estimate the velocity decay length to be between half and two filament lengths.

This is confirmed by an explicit calculation of the velocity correlation length from the velocity correlation function as outlined in fig. S6, fig. S7 and fig. S8. Moreover, the velocity correlation length is rather insensitive to a change in activity as was also found in Ref. [17], but does depend on the persistence length, see fig. S9.

For narrow bands, the velocity profiles of the two interfaces overlap, resulting in plug flow-type velocity profiles, as shown in fig. S3d. Note that in most cases the orientation of the filaments at the interface has a well-defined inclination angle ($15^\circ - 25^\circ$), see for example fig. S3a. Therefore motors between antiparallel filaments can only attach close to the filament ends and impose a pushing force from the rear end. Closer to the center of a band, the filaments are oriented parallel to the interface.

Fraction of antiparallel motors

Figure S4 shows the number n_m^{ap} of antiparallel motors per filament as a function of the total number of motors n_m in the system for three filament densities. In all cases, the number of antiparallel motors increases linearly with n_m and saturates at larger n_m where motors collide and detach from the filaments.

For systems evolving from the initial nematic state towards the buckling of bands, the number of antiparallel motors varies non-monotonically as a function of time for various persistence lengths. For very short times, the parallel and antiparallel orientations of neighbouring filaments are equiprobable and the fraction of antiparallel motors is $n_m^{\text{ap}}/n_m = 1/2$. Rapidly, thin bands (width a few filament thicknesses) appear and n_m^{ap}/n_m shoots up to almost unity (not shown), after which coarsening of the bands leads to a steady decrease of n_m^{ap} with time as is shown in fig. S5. As the active force is proportional to n_m^{ap} , fig. S5 also shows the time evolution of the force on the filaments. Interestingly, the curves for different persistence lengths follow the same time evolution, indicating that, at this stage, the microstructures are

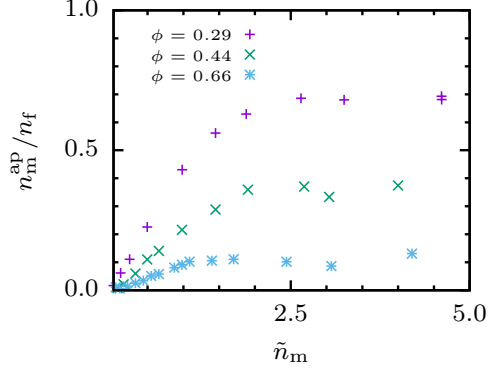


fig. S4. The number of antiparallel motors as a function of the total number of motors.
Here $(\phi, \tilde{\ell}_p, L/\sigma) = (0.66, 3.4, 20)$.

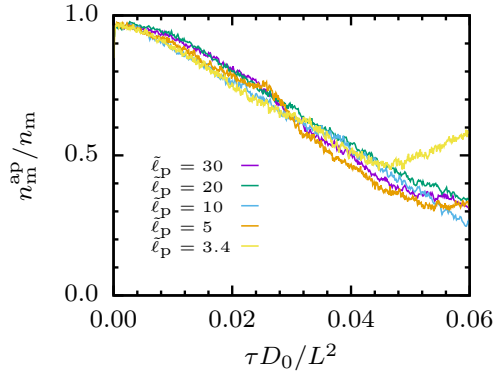


fig. S5. Time evolution of the number of antiparallel motors for different $\tilde{\ell}_p$.
Here $(\phi, \tilde{n}_m, L/\sigma) = (0.66, 1.0, 40)$. $\tau = 0$ corresponds to the initial disordered nematic state.

very similar.

Velocity correlation function

Additional comparison with existing experimental and simulation work [9,17] can be done through the spatial velocity correlation function

$$C_v(r, \tau) = \frac{\left\langle \sum_{i,j \neq i} \mathbf{d}_i(\tau) \cdot \mathbf{d}_j(\tau) \delta(r - |\mathbf{r}_i - \mathbf{r}_j|) \right\rangle_t}{\tau^2 \left\langle \sum_{i,j \neq i} \delta(r - |\mathbf{r}_i - \mathbf{r}_j|) \right\rangle_t}. \quad (1)$$

The center of mass displacement \mathbf{d}_i of filament i over a lag time τ is defined as $\mathbf{d}_i(\tau) = \mathbf{r}_i(t + \tau) - \mathbf{r}_i(t)$ with $\mathbf{r}_i(t)$ the center of mass of filament i at time t . The velocity $\mathbf{v} = \mathbf{d}(\tau)/\tau$ depends on the lag time τ . Examples of $C_v(r, \tau)$ for different activities at fixed lag time are shown in fig. S6a. The normalised velocity correlation

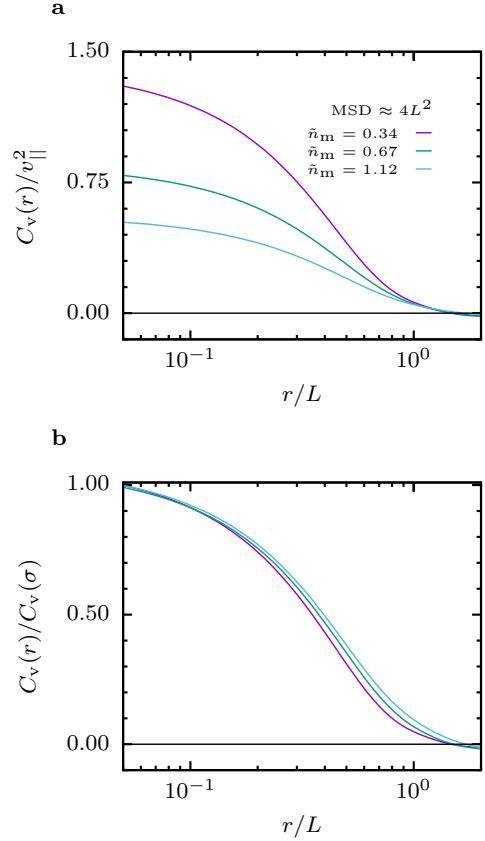


fig. S6. Filament velocity correlation functions.

Velocity correlation functions for three motor densities at $\tau/\tau_R^0 \approx 4$ with $(\phi, \tilde{\ell}_p) = (0.66, 3.4)$. (a) Unnormalized correlation functions, nondimensionalised by the parallel velocity v_{\parallel}^2 . (b) Normalised correlation functions.

function at a particular lag time in fig. S6b is essentially independent of the activity, which is consistent with previous experimental and numerical studies [9,17]. The lag time τ has to be rescaled to compare MSD, $v_{\parallel}(\tau)$ and correlation functions for different parameter sets. The rescaled time evolution displayed in fig. S7 suggests that L/v_{\parallel} is the natural intrinsic time scale, so that $\tau v_{\parallel}/L$ is the appropriate scaling variable for the active ballistic regime where $\text{MSD} \propto v_{\parallel}^2 \tau^2$.

To gain more understanding, we focus on $r > \sigma$ and lag times τ , such that the passive system is in the diffusive regime (in fig. S7, this corresponds to the time window in which the scaled MSDs overlap). In this case, long-ranged spatial correlations build up [43] and $C_v(r, \tau)$ typically shows an exponential decay [44], $C_v(r, \tau) = A \exp[-r/\xi]$.

The amplitude A and velocity correlation length ξ are shown in fig. S8a and b, respectively, for different activities (changing the number of motors, while keeping all other parameters constant). Spatial velocity correla-

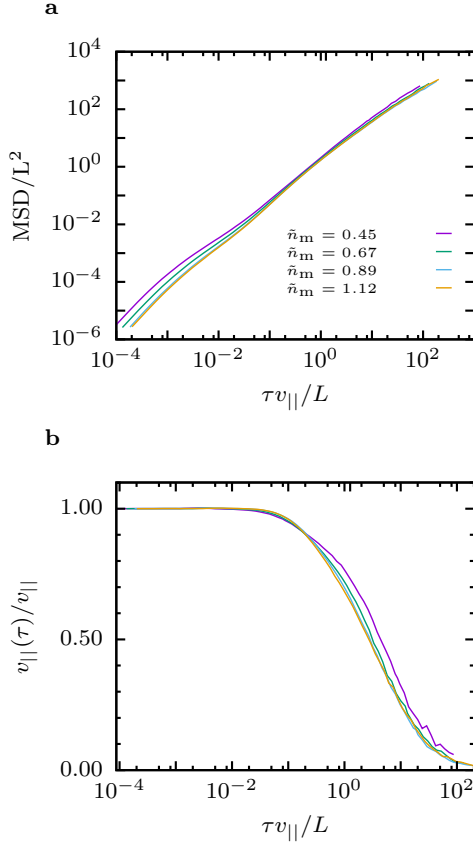


fig. S7. Time scale renormalization for active motion. (a) MSD for different motor concentrations and (b) scaled parallel velocity for different motor concentrations. In both cases $(\phi, \ell_p) = (0.66, 3.4)$. Note that $v_{||}(\tau)$ refers to the time-dependent quantity and $v_{||} = v_{||}(\tau = 0)$.

tions build up at short times and decay at long times. A maximum amplitude is found at $\tau v_{||}/L \approx 1/2$, the time at which filaments have moved about half their length. Interestingly, the time-dependent velocity correlation lengths ξ/L for different activities superimpose when plotted as a function of $\tau v_{||}/L$. The same behaviour of the velocity correlation length is also found when the area fraction of filaments is changed, as shown in fig. S8c, except for very small area fractions ($\phi < 0.3$) where the filaments are still in the isotropic state (see the snapshots in fig. 6 a,b in the main text).

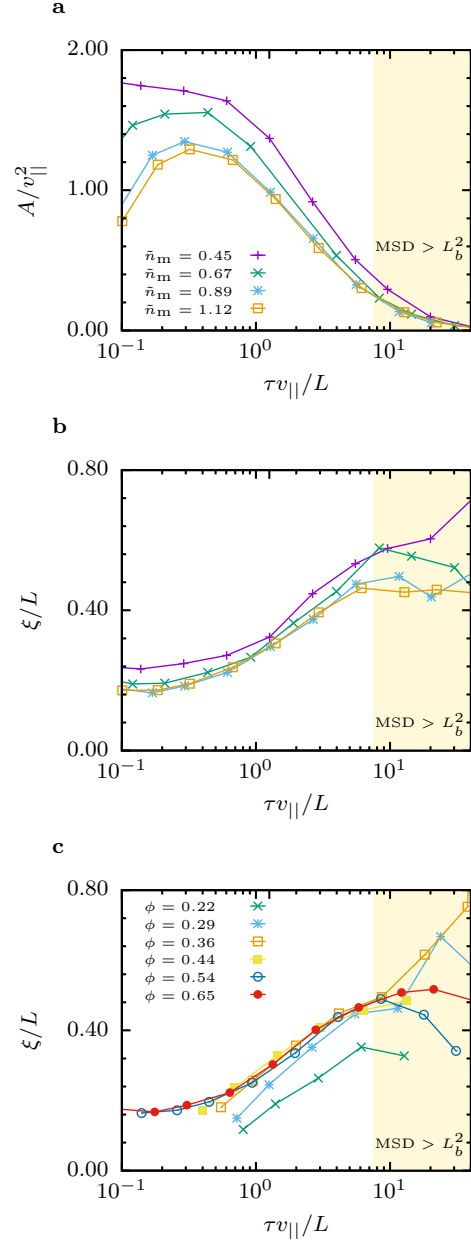


fig. S8. Amplitude and decay length of the velocity correlation function as a function of the lag time. (a,b) Varying the motor density $0.4 < \bar{n}_m < 1.5$, with $(\phi, \ell_p) = (0.66, 3.4)$, (a) Amplitude, (b) Velocity decay length. (c) Velocity decay length for different area fractions with $(\ell_p, \bar{n}_m) = (3.4, 0.89)$.

However, a different behaviour is found when the filament persistence length is varied, see fig. S9; here the velocity correlation length ξ increases with increasing filament stiffness and saturates to a constant value of approximately $\xi/\ell_p \approx 0.04$ for large persistence lengths, see fig. S9a. However, for small persistence lengths $\ell_p \approx L$,

where domain sizes are small, the velocity correlation length is independent of ℓ_p and approaches a constant $\xi/L = 0.16$ for $\tau v_{\parallel}/L = 1/2$, see fig. S9b. As for most of the results discussed we have focussed on systems with a fixed aspect ratio $L/\sigma = 20$. We also included simulation data for longer filaments $L/\sigma = 40$ which show that the scaling proposed in fig. S9 is reasonable but might be more complicated as the filament thickness is ignored.

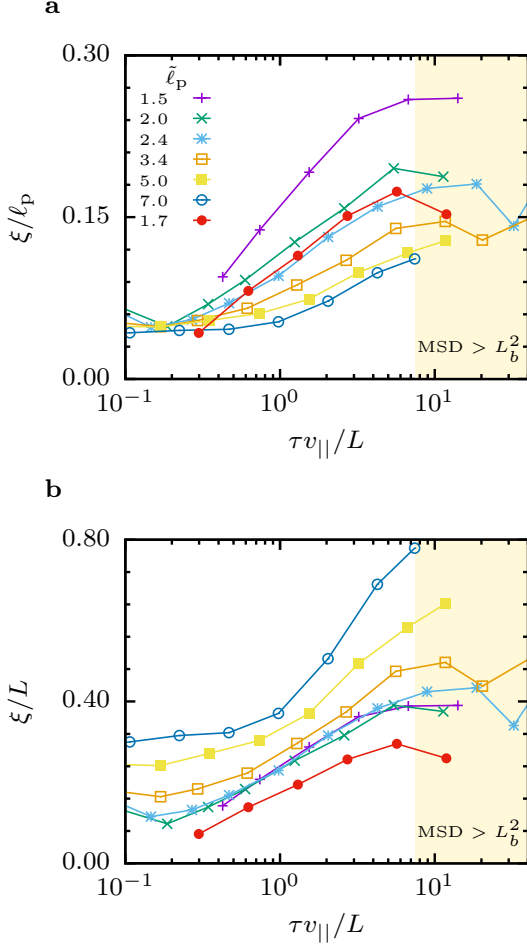


fig. S9. Dependence of the velocity correlation length on the persistence length.

(a) Normalisation of ξ by the persistence length ℓ_p , (b) Normalisation of ξ by the filament length L . Here all simulations are for $L/\sigma = 20$, except for the filled red symbols which are for $L/\sigma = 40$.

Our system is different from the experiments in Ref. [9], where suspensions of extensile bundles of microtubules and kinesin motors are studied and in which the velocity correlations are measured using displacements of large tracer particles. It is also different from the continuum model of Ref. [17] based on the theory of active nematics. Nevertheless, the velocity correlation functions are in all cases found to be exponential functions, and

in particular the correlation length is rather insensitive to the activity. Moreover, for larger filament stiffnesses $\ell_p \gg L$ we also find an approximately linear increase of the velocity correlation length with increasing bending rigidity (in our case $\tilde{\ell}_p$) as in active gel theory [17]. For small filament stiffness our component-based model predicts universal scaling for ξ/L for various persistence lengths.

Spatial orientational correlation function

The sizes of the domains can be estimated through the segment-based spatial orientational correlation functions, $\Omega_{\parallel}(r)$ and $\Omega_{\perp}(r)$, which measure the average angle between filament segments found at a distance r from a central segment parallel or perpendicular to the orientation of that central segment,

$$\Omega_{\parallel}(r) = \left\langle \frac{\sum_{s,j} \delta(\hat{\mathbf{p}}_q^i \cdot \hat{\mathbf{r}}_{qs}^{ij} - 1) \delta(|\mathbf{r}_{qs}^{ij}| - r) \arccos(\hat{\mathbf{p}}_q^i \cdot \hat{\mathbf{p}}_s^j)}{\sum_{s,j} \delta(\hat{\mathbf{p}}_q^i \cdot \hat{\mathbf{r}}_{qs}^{ij} - 1) \delta(|\mathbf{r}_{qs}^{ij}| - r)} \right\rangle_{q,i,t}$$

and

$$\Omega_{\perp}(r) = \left\langle \frac{\sum_{s,j} \delta(\hat{\mathbf{p}}_q^i \cdot \hat{\mathbf{r}}_{qs}^{ij}) \delta(|\mathbf{r}_{qs}^{ij}| - r) \arccos(\hat{\mathbf{p}}_q^i \cdot \hat{\mathbf{p}}_s^j)}{\sum_{s,j} \delta(\hat{\mathbf{p}}_q^i \cdot \hat{\mathbf{r}}_{qs}^{ij}) \delta(|\mathbf{r}_{qs}^{ij}| - r)} \right\rangle_{q,i,t}$$

Here, $\sum_{s,j}$ is a short notation for the double sum $\sum_s \sum_j$; the delta functions select the distances and orientations. The unit orientation vector of a segment is $\hat{\mathbf{p}}_q^i = (\mathbf{r}_q^{i+1} - \mathbf{r}_q^i) / |\mathbf{r}_q^{i+1} - \mathbf{r}_q^i|$, the separation between two segments i, j on filaments q, s is $r = |\mathbf{r}_{qs}^{ij}| = |(\mathbf{r}_q^i + \mathbf{r}_q^{i+1}) - (\mathbf{r}_s^j + \mathbf{r}_s^{j+1})|/2$, and $\hat{\mathbf{r}}_{qs}^{ij} = \mathbf{r}_{qs}^{ij} / |\mathbf{r}_{qs}^{ij}|$ is the unit separation vector.

The functions $\Omega_{\parallel}(r)$ and $\Omega_{\perp}(r)$ are zero for small distances and saturate to $\pi/2$ at large distances, where parallel and antiparallel orientations are equally probable. Therefore, the displaced and normalised functions $\hat{\Omega}(r) = 1 - 2\Omega(r)/\pi$ decay rapidly as shown in fig. S10.

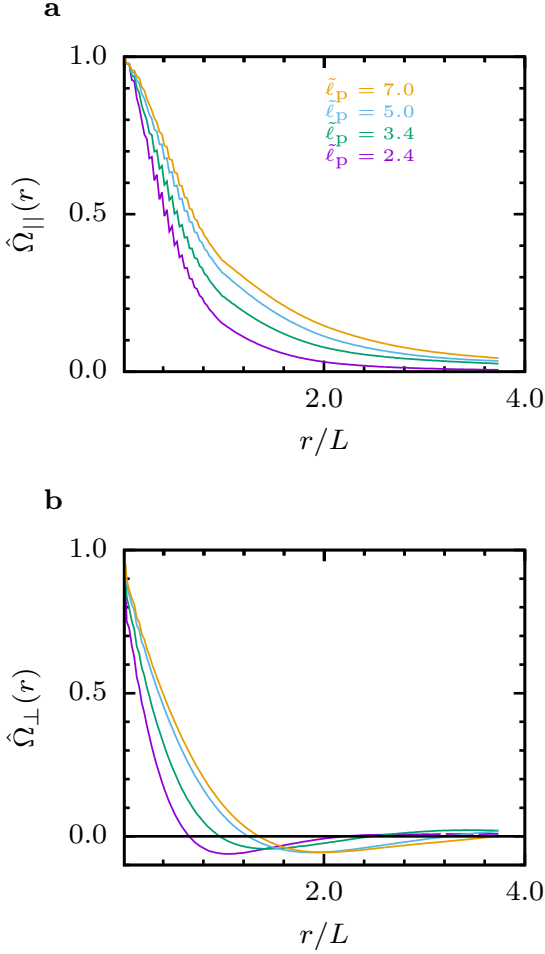


fig. S10. Segment orientational correlation functions for filaments with various persistence lengths. (a) Longitudinal $\hat{\Omega}_{\parallel}(r)$, and (b) transversal $\hat{\Omega}_{\perp}(r)$ for $(\phi, \tilde{n}_m) = (0.66, 0.89)$.

This decay allows the estimation of the domain sizes parallel and perpendicular to the filament orientation. The length l_{\parallel} and the width l_{\perp} are defined as twice the peak width at half maximum. The examples of $\hat{\Omega}(r)$ displayed in fig. S10 show that the decay length decreases when the persistence length decreases, i.e., domains become smaller. The transversal orientational correlation function shows oscillations, indicating the abrupt change of the orientation when the interface between domains is crossed.

Effective persistence length

We study the effect of activity and concentration on the effective filament stiffness or effective persistence length ℓ_p^* . This effective persistence length is calculated by an exponential fit of the tangent correlation function (see

fig. S11a) in the motor-filament mixture at filament concentration ϕ and motor concentration \tilde{n}_m . The calculations show that for increasing motor concentrations the exponential decay is faster and the effective persistence length smaller, see fig. S11b. In fig. S11b we show that ℓ_p^* follows a universal scaling for with the active force for large enough activities. However, this universality breaks down if the density is small, in particular for $\phi < 0.29$. The square-root dependence of the effective persistence on the activity is weaker than the square dependence found by Joshi *al.* [26] but consistent with the scaling that we find for other length scales.

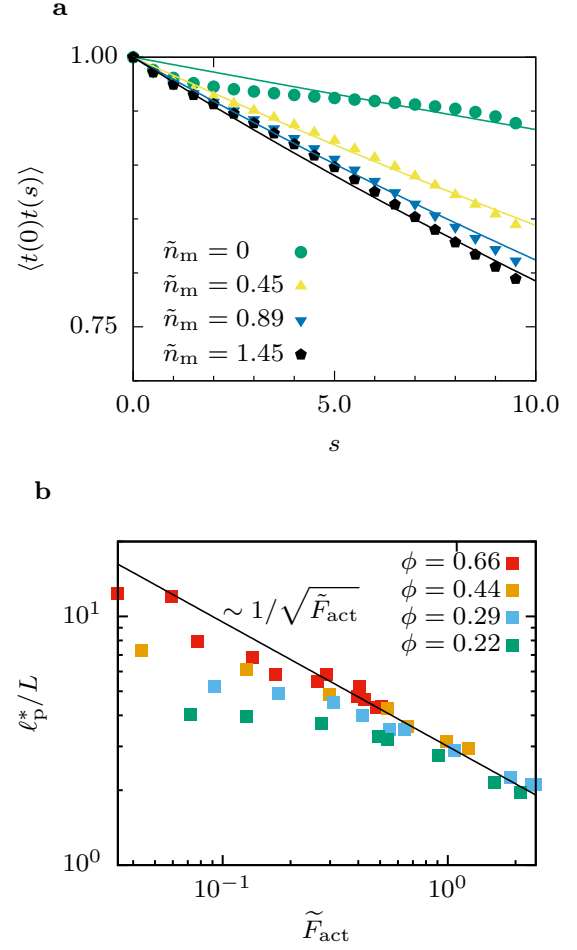


fig. S11. Effective persistence length (a) Tangent correlation functions for different motor concentrations for $(\phi, \tilde{\ell}_p) = (0.66, 3.4)$. (b) Effective persistence length for different filament concentrations for $(\tilde{n}_m, \tilde{\ell}_p) = (0.89, 3.4)$.

Movie captions

Movie S1: Dynamics of polarity sorting and coarsening of polar bands from the initial disordered nematic state.

The parameters are $(\phi, \tilde{\ell}_p, \tilde{n}_m) = (0.66, 5, 0.89)$. The duration of the movie is $\tilde{t} \approx 2.7\tau_R^0$ (500 frames, sampling every 200 time steps).

Movie S2: Steady state dynamics of polar domains with repeated creation and annihilation of defect pairs.

Here $(\phi, \tilde{\ell}_p, \tilde{n}_m) = (0.66, 3.4, 0.89)$. The duration of the movie is $\tilde{t} \approx 13.5\tau_R^0$ (500 frames, sampling every 1000 time steps).

Movie S3: Dynamics of the elastic instability.

Formation and buckling of polar bands leads to the

emergence of the disordered phase. Here the parameters are $(\phi, L/\sigma, \tilde{\ell}_p, \tilde{n}_m) = (0.66, 40, 10, 1.0)$. The duration of the movie is $\tilde{t} \approx 2\tau_R^0$ (800 frames, sampling every 500 time steps).

Movie S4: Defect dynamics.

Extensile motion of a $\pm 1/2$ defect pair. The $-1/2$ defect (purple) is nearly immobile, the $+1/2$ defect (blue) moves. Here the parameters are $(\phi, \tilde{\ell}_p, \tilde{n}_m) = (0.66, 5, 0.89)$. The duration of the movie is $\tilde{t} \approx 2.2\tau_R^0$. This movie is clipped from a larger field of view (70 frames, sampling every 2000 time steps).

Movie S5: Defect annihilation.

Annihilation of a $+1/2$ (blue) and $-1/2$ defect (purple). The parameters are $(\phi, \tilde{\ell}_p, \tilde{n}_m) = (0.66, 5, 0.89)$. The duration of the movie is $\tilde{t} \approx 2.2\tau_R^0$. This movie is clipped from a larger field of view (70 frames, sampling every 2000 time steps).

REFERENCES AND NOTES

1. M. C. Marchetti, J. F. Joanny, S. Ramaswamy, T. B. Liverpool, J. Prost, M. Rao, R. A. Simha, Hydrodynamics of soft active matter. *Rev. Mod. Phys.* **85**, 1143 (2013).
2. S. E. Spagnolie, *Theory of Active Suspensions* (Springer Science+Business Media, 2015), chap. 9, 319 p.
3. J. Elgeti, R. G. Winkler, G. Gompper, Physics of microswimmers—Single particle motion and collective behavior: A review. *Rep. Prog. Phys.* **78**, 056601 (2015).
4. A. Doostmohammadi, J. Ignés-Mullol, J. M. Yeomans, F. Sagués, Active nematics. *Nat. Commun.* **9**, 3246 (2018).
5. D. A. Fletcher, R. D. Mullins, Cell mechanics and the cytoskeleton. *Nature* **463**, 485–492 (2010).
6. C. Lin, M. Schuster, S. C. Guimaraes, P. Ashwin, M. Schrader, J. Metz, C. Hacker, S. J. Gurr, G. Steinberg, Active diffusion and microtubule-based transport oppose myosin forces to position organelles in cells. *Nat. Commun.* **7**, 11814 (2016).
7. W. Lu, M. Winding, M. Lakonishok, J. Wildonger, V. I. Gelfand, Microtubule-microtubule sliding by kinesin-1 is essential for normal cytoplasmic streaming in drosophila oocytes. *Proc. Natl. Acad. Sci. U.S.A.* **113**, E4995–E5004 (2016).
8. F.-C. Tsai, B. Stuhrmann, G. H. Koenderink, Encapsulation of active cytoskeletal protein networks in cell-sized liposomes. *Langmuir* **27**, 10061–10071 (2011).
9. T. Sanchez, D. T. N. Chen, S. J. DeCamp, M. Heymann, Z. Dogic, Spontaneous motion in hierarchically assembled active matter. *Nature* **491**, 431–434 (2012).
10. F. C. Keber, E. Loiseau, T. Sanchez, S. J. DeCamp, L. Giomi, M. J. Bowick, M. C. Marchetti, Z. Dogic, A. R. Bausch, Topology and dynamics of active nematic vesicles. *Science* **345**, 1135–1139 (2014).
11. G. Henkin, S. J. DeCamp, D. T. N. Chen, T. Sanchez, Z. Dogic, Tunable dynamics of microtubule-based active isotropic gels. *Phil. Trans. R. Soc. A* **372**, 20140142 (2014).
12. P. Guillamat, J. Ignés-Mullol, F. Sagués, Taming active turbulence with patterned soft interfaces. *Nat. Commun.* **8**, 564 (2017).
13. N. Kumar, R. Zhang, J. J. de Pablo, M. L. Gardel, Tunable structure and dynamics of active liquid crystals. *Sci. Adv.* **4**, eaat7779 (2018).
14. L. Giomi, M. J. Bowick, P. Mishra, R. Sknepnek, M. C. Marchetti, Defect dynamics in active nematics. *Phil. Trans. R. Soc. A* **372**, 20130365 (2014).

15. L. Giomi, Geometry and topology of turbulence in active nematics. *Phys. Rev. X* **5**, 031003 (2015).
16. T. Gao, R. Blackwell, M. A. Glaser, M. D. Betterton, M. J. Shelley, Multiscale polar theory of microtubule and motor-protein assemblies. *Phys. Rev. Lett.* **114**, 048101 (2015).
17. S. P. Thampi, R. Golestanian, J. M. Yeomans, Velocity correlations in an active nematic. *Phys. Rev. Lett.* **111**, 118101 (2013).
18. S. P. Thampi, R. Golestanian, J. M. Yeomans, Vorticity, defects and correlations in active turbulence. *Phil. Trans. R. Soc. A* **372**, 20130366 (2014).
19. A. Doostmohammadi, M. F. Adamer, S. P. Thampi, J. M. Yeomans, Stabilization of active matter by flow-vortex lattices and defect ordering. *Nat. Commun.* **7**, 10557 (2016).
20. E. J. Hemingway, P. Mishra, M. C. Marchetti, S. M. Fielding, Correlation lengths in hydrodynamic models of active nematics. *Soft Matter* **12**, 7943–7952 (2016).
21. T. Gao, M. D. Betterton, A.-S. Jhang, M. J. Shelley, Analytical structure, dynamics, and coarse graining of a kinetic model of an active fluid. *Phys. Rev. Fluids* **2**, 093302 (2017).
22. I. Maryshev, D. Marenduzzo, A. B. Goryachev, A. Morozov, Kinetic theory of pattern formation in mixtures of microtubules and molecular motors. *Phys. Rev. E* **97**, 022412 (2018).
23. R. A. Simha, S. Ramaswamy, Hydrodynamic fluctuations and instabilities in ordered suspensions of self-propelled particles. *Phys. Rev. Lett.* **89**, 058101 (2002).
24. D. Saintillan, M. J. Shelley, Instabilities and pattern formation in active particle suspensions: Kinetic theory and continuum simulations. *Phys. Rev. Lett.* **100**, 178103 (2008).
25. S. J. DeCamp, G. S. Redner, A. Baskaran, M. F. Hagan, Z. Dogic, Orientational order of motile defects in active nematics. *Nat. Mater.* **14**, 1110–1115 (2015).
26. A. Joshi, E. Putzig, A. Baskaran, M. F. Hagan, The interplay between activity and filament flexibility determines the emergent properties of active nematics. *Soft Matter* **15**, 94–101 (2018).
27. D. A. Head, W. J. Briels, G. Gompper, Spindles and active vortices in a model of confined filament-motor mixtures. *BMC Biophysics* **4**, 18 (2011).
28. T. Gao, R. Blackwell, M. A. Glaser, M. D. Betterton, M. J. Shelley, Multiscale modeling and simulation of microtubule–motor-protein assemblies. *Phys. Rev. E* **92**, 062709 (2015).
29. R. Blackwell, O. Sweezy-Schindler, C. Baldwin, L. E. Hough, M. A. Glaser, M. D. Betterton, Microscopic origins of anisotropic active stress in motor-driven nematic liquid crystals. *Soft Matter* **14**, 2676–2687 (2016).

30. A. Ravichandran, G. A. Vliegenthart, G. Saggiorato, T. Auth, G. Gompper, Enhanced dynamics of confined cytoskeletal filaments driven by asymmetric motors. *Biophys. J.* **113**, 1121–1132 (2017).
31. V. Narayan, S. Ramaswamy, N. Menon, Long-lived giant number fluctuations in a swarming granular nematic. *Science* **317**, 105–108 (2007).
32. X.-q. Shi, Y.-q. Ma, Topological structure dynamics revealing collective evolution in active nematics. *Nat. Commun.* **4**, 3013 (2013).
33. E. Putzig, G. S. Redner, A. Baskaran, A. Baskaran, Instabilities, defects, and defect ordering in an overdamped active nematic. *Soft Matter* **12**, 3854–3859 (2016).
34. J. R. Howse, R. A. L. Jones, A. J. Ryan, T. Gough, R. Vafabakhsh, R. Golestanian, Selfmotile colloidal particles: From directed propulsion to random walk. *Phys. Rev. Lett.* **99**, 048102 (2007).
35. T. Odijk, Elastic constants of nematic solutions of rod-like and semi-flexible polymers. *Liq. Cryst.* **1**, 553–559 (1986).
36. R. Wittmann, C. E. Sitta, F. Smallenburg, H. Löwen, Phase diagram of two-dimensional hard rods from fundamental mixed measure density functional theory. *J. Chem. Phys.* **147**, 134908 (2017).
37. R. E. Isele-Holder, J. Elgeti, G. Gompper, Self-propelled worm-like filaments: Spontaneous spiral formation, structure and dynamics. *Soft Matter* **11**, 7181–7190 (2015).
38. S. Fürthauer, B. Lemma, P. J. Foster, S. C. Ems-McClung, C.-H. Yu, C. E. Walczak, Z. Dogic, D. J. Needleman, M. J. Shelley, Self-straining of actively crosslinked microtubule networks. *Nat. Phys.* **15**, 1295–1300 (2019).
39. B. Martínez-Prat, J. Ignés-Mullol, J. Casademunt, F. Sagués, Selection mechanism at the onset of active turbulence. *Nat. Phys.* **15**, 362–366 (2019).
40. N. Grønbech-Jensen, O. Farago, A simple and effective Verlet-type algorithm for simulating Langevin dynamics. *Mol. Phys.* **111**, 983–991 (2013).
41. J. Kierfeld, O. Niamploy, V. Sa-yakanit, R. Lipowsky, Stretching of semiflexible polymers with elastic bonds. *Eur. Phys. J. E* **14**, 17–34 (2004).
42. J. A. Barker, D. Henderson, What is “liquid”? Understanding the states of matter. *Rev. Mod. Phys.* **48**, 587 (1976).
43. B. Doliwa, A. Heuer, Cooperativity and spatial correlations near the glass transition: Computer simulation results for hard spheres and disks. *Phys. Rev. E* **61**, 6898 (2000).

44. A. Wysocki, R. G. Winkler, G. Gompper, Cooperative motion of active Brownian spheres in three-dimensional dense suspensions. *Europhys. Lett.* **105**, 48004 (2014).